Quasi Monostatic versus Near Forward Scatter geometry in WiFi-based passive radar sensors

Fabiola Colone, Tatiana Martelli, Pierfrancesco Lombardo

Abstract— **In this paper the comparison is investigated between quasi-monostatic and near forward scatter configurations for WiFi-based passive radar sensors. To this purpose, a barrier coverage application for vehicular targets is considered as a possible implementation of the conceived green sensor within surface transportation monitoring solutions. The performance of the two alternative sensor geometries are compared by means of theoretical and experimental analysis as well as based on considerations on the practical implementation. The reported results provide a realistic characterization of the performance of a bistatic radar sensor to be exploited in barrier coverage problems and give indications for the design of such a system. The specific demonstration with WiFi-based passive radar aims at extending the use of this emerging technology to perimeter monitoring applications for vehicular targets, exploiting the near forward scatter geometry.**

Index Terms— **passive bistatic radar, forward scattering radar, barrier coverage, perimeter surveillance, intrusion detection.**

I.   INTRODUCTION

In the last decades, there has been a great interest in passive radar sensors that exploit existing transmitters as illuminators of opportunity [1]-[3]. Specifically the parasitic exploitation of IEEE 802.11 (WiFi) transmissions has been shown to be an effective solution for local area surveillance applications. To this purpose, many signal processing techniques and operative strategies have been devised to enable the detection, localization and imaging of vehicles and human beings by means of WiFi-based passive radar sensors [4]-[11].

However, the practical demonstration of the effectiveness of such methods has been typically performed under conventional acquisition geometries. Specifically quasi-monostatic (QMS) and moderate bistatic (BS) configurations have been usually exploited in many reported studies. For the sake of clearness, in a QMS geometry, the angle subtended between transmitter (Tx), target and receiver (Rx), namely the bistatic angle, is close to zero so that the Tx-Rx pair operates close to a monostatic radar sensor. In contrast, in a BS geometry, the bistatic angle is not negligible; anyway, in the mentioned studies, it was typically lower than 45 degrees. The exploitation of such typical geometries is mainly motivated by the need to preserve the range and velocity resolution offered by the exploited waveform of opportunity, which can be shown to rapidly degrade as the bistatic angle increases exceeding 45 degrees [12]. Therefore, by exploiting QMS or moderate BS geometries

potentially enables an accurate localization of the detected targets.

In specific applications, range resolution could be traded for an enhanced capability to detect the target. This is the case of surveillance applications such as intrusion detection and border control, in which the capability to cover a continuous barrier spanning the protected region becomes the critical problem.

In such applications, the exploitation of extreme bistatic configurations has been considered based on the forward scatter radar principle [12]. Basically, by exploiting bistatic angles close to 180 degrees, the radar designer sacrifices the capability to accurately localize the target for the benefits yield by the "forward scattering" mechanism. This is invoked to model the energy scattered by the target as it crosses the Tx-Rx baseline. If properly exploited, this effect results in a number of advantages compared to traditional monostatic or moderate bistatic geometries, such as enhanced target radar cross-section (RCS), robustness to stealth technology, limited hardware complexity and improved automatic target classification [13]. After the renewed interest received in active radar applications, there has been a growing attention to the use of forward scatter configurations also in passive radar [14]-[19]. Recently, the potential of a WiFi-based passive radar in forward scatter configuration has been investigated for vehicle classification by the authors in [20].

However, with particular reference to a WiFi-based passive radar, due to both the short range coverage and the reasonably high carrier frequencies (ISM band at 2.4 GHz), the benefits of a forward scatter geometry in the strictest sense will be experienced only in a very limited portion of the target's crossing path, namely within close proximity to the Tx-Rx baseline. Therefore, aiming at the construction of a barrier with sufficient thickness, namely a belt barrier rather than a line barrier, in order to minimize the vulnerability of the protected region, near forward scatter (NFS) configurations have to be considered. Specifically, with such expression we refer to bistatic geometries where the bistatic angle exceeds 90 degrees and approaches (but does not reach) 180 degrees so that the Tx-Rx pair operates close to a forward scatter radar.

It is then interesting to characterize the potential benefits conveyed by such NFS geometry in order to understand whether it partially retains the advantageous characteristic of a strict forward scatter geometry when compared to conventional QMS sensors configurations.

F. Colone, T. Martelli, and P. Lombardo are with the DIET Dept. of Sapienza University of Rome, Italy (e-mail: fabiola.colone@uniroma1.it, martelli@diet.uniroma1.it, pierfrancesco.lombardo@uniroma1.it).

Therefore, this work focuses on the comparison between the QMS sensors geometry and the NFS sensors geometry for barrier coverage applications. Our comparison is carried out with respect to two main points:

(i) Target detection performance: This point is crucial in the design of a specific coverage, because it is required to define the main parameters for the Tx and Rx nodes (transmitted power, antenna characteristics, receiver noise figure, …) so that target with desired characteristics (size, material, RCS, …) is detected with the desired performance (e.g. false alarm probability, P_{fa}, and detection probability, P_d). It is also important to assess the relative performances of QMS and NFS configurations. This determines the sensors geometry to select when it is possible to choose between the two configurations to cover a specific region. Also, when sensors in both configurations must operate together and the transmitted power is assigned, the sensors network topology has to be designed in accordance with the performance provided by different types of sensors and might be driven by the sensor with poorest performance.

(ii) Computational cost of the detection scheme: this second point is related to the cost of the receiving sensors, where the processing algorithms are implemented. In the case of comparable detection performance, a sensibly lower cost for one of the two types of sensor configurations would suggest to select this type when a choice is possible. In addition, if the two configurations are to be used within a unique surveillance system, so that the sensor with the worst performance leads the system geometry design, it is very sensible to reduce the computational cost of the other one, by accepting a detection performance reduction that balances it against the other.

While a fraction of the above mentioned comparison can be performed based on geometrical and theoretical analysis, another fraction requires a dedicated experimental analysis to avoid making ideal (possibly unrealistic) assumptions especially with regards to the scattering models. Also, despite some results have a wider applicability, the validation of both QMS and NFS configuration results is considered potentially relevant for a significant case inside the surface-based vehicular traffic monitoring application. In order to provide such a real world application, numerical examples and experimental results are reported for the case of a WiFi-based passive radar sensor employed in perimeter monitoring of surface vehicles.

The analysis of the first point of the comparison is conducted in Section II in terms of a theoretical power budget computation by means of the well-known bistatic radar equation. Both a free-space model and a two-ray path model are exploited in order to investigate the impact of multipath on the reported comparison. The theoretical results clearly show that the NFS configuration is to be preferred even when assuming that the scattering characteristics of the target are angle-invariant.

This simplifying hypothesis is then removed by comparing the considered geometries in terms of induced target RCS behavior. To this purpose, in Section III we describe an experimental campaign that has been conducted to simultaneously collect data by two WiFi-based passive radar receivers exploiting respectively a QMS and a NFS configuration. Section IV reports the results obtained by processing such simultaneously acquired data sets. Notice that, as the focus is the comparison of the sensors geometries, no attempt is made to optimize the processing techniques for each considered case. Therefore, existing processing schemes are employed, previously developed by the authors [5][7]. The analysis clearly demonstrates the RCS enhancement resulting from the exploitation of a NFS geometry for a number of tests employing vehicular targets. By averaging on the available data set, a rough but reliable quantification of this enhancement is obtained.

Section V is dedicated to a comparative analysis of the computational loads required by the two types of sensors. It if first observed that the adopted acquisition geometry has a non-negligible impact on the processing strategies employed by the considered sensor. This is followed by a detailed comparative study of QMS and NFS configurations in terms of the complexity of the required processing stages. Again, the NFS geometry is shown to offer superior performance in term of sensor cost avoidance since it sets looser constraints on both the computational load and storage capability. Moreover, with particular reference to the WiFi-based passive radar tests, we show that the inherent detection performance enhancement can be nicely traded with a further reduction of the system complexity. This is obtained by properly adjusting the parameters of the employed processing techniques for the considered geometry.

Detailed conclusions are drawn in section VI, which summarizes the results of the comparison between QMS and NFS configurations. Together with the general results, showing a preference for the NFS sensors geometry, this manuscript also shows that a surveillance system for vehicular surface traffic can be nicely implemented using WiFi-based passive radar sensors operating in both QMF and NFS configurations, which is also a contribution of this paper.

II. QUASI-MONOSTATIC VS. NEAR FORWARD SCATTER GEOMETRY: A POWER BUDGET COMPARISON

The acquisition geometries compared in this paper are illustrated in Figure 1 with reference to the considered application. It is assumed that the detection of intruders is sought in a rectangular cuboid with base of length D, width W, and heigh H; this volume can be interpreted as a portion of a continuous belt barrier with some breadth or just as a gateway to a protected area. In both cases the system should provide coverage against any crossing path, namely a path that connects one side of the region (i.e. entrance side) to the opposite side (i.e. exit side).

A Cartesian coordinate system is adopted in the following; its origin is located right in the middle of the region, the horizontal xy plane lies on the ground being the x-axis parallel to the longest side of the region, and the z-axis points upward.
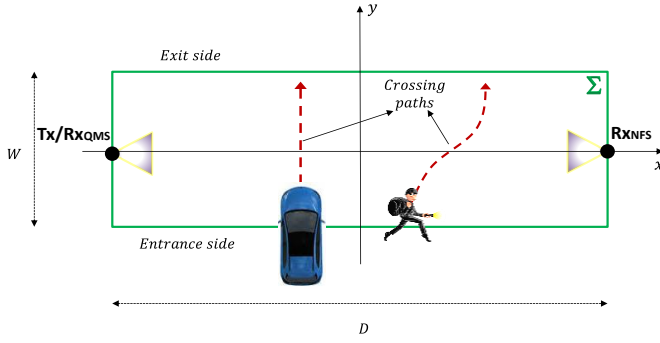
Figure 1. Sketch of the considered scenario and radar acquisition geometries under analysis: quasi-monostatic (QMS) vs near forward scatter (NFS).

We assume the transmitter (Tx) to be located at $\Omega_{Tx} \equiv (-D/2, 0, H_{Tx})^T$, i.e. at the mid-point of one of the shortest sides of the rectangle.

The QMS geometry exploits a receiver (Rx$_{QMS}$) that is almost co-located with the Tx. For the sake of simplicity we assume that its position is given by $\Omega_{Rx_{QMS}} \equiv (-D/2, 0, H_{Rx_{QMS}})^T$, being the Tx and Rx antennas possibly displaced in the vertical direction only.

The NFS geometry employs a receiver (Rx$_{NFS}$) that is arranged at $\Omega_{Rx_{NFS}} \equiv (D/2, 0, H_{Rx_{NFS}})^T$ so that the bistatic radar baseline is parallel to the x-axis; it is orthogonal to the shortest segments connecting up- and down-boundary of the considered region and symmetrically located with respect to the region width.

For a fair comparison, we assume that the QMS and NFS sensors employ identical sensors, there including the adopted antennas.

In order to provide a preliminary performance comparison between the two geometries in term of power budget, we resort to the well-known bistatic radar equation [21] so that the power received from a target can be expressed as:

$$P_{Rx} = P_{Tx} G_{Tx} G_{Rx} \frac{4\pi\sigma}{\lambda^2} L_{Tx} L_{Rx} \qquad (1)$$

where, despite not explicitly shown, many parameters are function of the sensor/target geometry as described below. Specifically
- P_{Tx} is the transmitted power;
- G_{Tx} and G_{Rx} are the Tx and Rx antenna gains, respectively, and depend on the employed antennas, their position and mechanical steering, and are functions of the target coordinates $\Omega \equiv (x, y, z)^T$;
- σ is the target radar cross section (RCS) that is characteristic of the target itself but also depends on the observation geometry via the bistatic angle, namely the angle subtended between the Tx, target and Rx, and the target aspect angle;
- λ is the wavelength;
- L_{Tx} and L_{Rx} account for the propagation losses on the Tx-to-target and target-to-Rx paths, respectively.

Moreover, we neglect the dependence of the RCS on the target aspect angle, namely the angle between the major axis of the target (usually coincident with the heading direction) and the radar line of sight (LOS), i.e. the direction of the bistatic angle bisector.

In this section, we are interested to investigate only the effect of the Tx-target-Rx geometry on the expected power budget. To this purpose we deliberately exclude the target RCS from the following analysis by setting its value to a constant in order to highlight the effect of all the other relevant parameters in the radar equation. In other words we assume the target has an isotropic RCS pattern. In particular, we make the ideal assumption that the scattering characteristics of the target are independent of the bistatic angle.

This allows us to perform a preliminary comparison between the two alternative sensors configurations without relying on any specific assumption about the target response observed under the two different geometries. The complementary comparison between the QMS and the NFS geometries in term of observable target RCS is reported in Section IV where the ideal assumption is removed.

Here we focus solely on the variation of the received power level with the target position within the region defined in Figure 1, i.e. $\Omega \in \Sigma \equiv \left\{ \Omega \text{ s.t. } |x| \leq \frac{D}{2} \text{ ; } |y| \leq \frac{W}{2}; \ 0 \leq z \leq H \right\}$. In particular, as the target detection has to be guaranteed all around the strip region Σ of Figure 1, we use the worst case condition as a reasonable performance metric:

$$S_{Rx} = \min_{\Omega \in \Sigma}\{P_{Rx}\} = P_{Tx} \frac{4\pi\sigma}{\lambda^2} \min_{\Omega \in \Sigma}\{G_{Tx} G_{Rx} L_{Tx} L_{Rx}\} \qquad (2)$$

By indicating with $G_{Rx_{NFS}}$ and $G_{Rx_{QMS}}$ the Rx antenna gain (G_{Rx}) provided by the QMS and the NFS sensors, respectively, a direct comparison between the two alternative geometries is then provided by the ratio:

$$\Delta S_{NFS/QMS} = \frac{S_{Rx_{NFS}}}{S_{Rx_{QMS}}} = \frac{\min_{\Omega \in \Sigma}\{G_{Tx} G_{Rx_{NFS}} L_{Tx} L_{Rx_{NFS}}\}}{\min_{\Omega \in \Sigma}\{G_{Tx} G_{Rx_{QMS}} L_{Tx} L_{Rx_{QMS}}\}} \qquad (3)$$

which can be regarded as the signal-to-noise ratio (SNR) gain provided by the NFS configuration with respect to the QMS geometry. Notice that, despite the Tx-to-target geometry is in common, the factors related to the Tx antenna cannot be simplified as the worst case condition for the NFS and the QMS sensors do not occur at the same target position.

Following the approach in [22], we carry out the power budget comparison with reference to two different propagation models: the free-space model and the two-ray path (TRP) model.

A. Free-space propagation model

Under the assumption of a free space propagation model, the propagation losses in (1) are readily defined as $L_{Tx} = (\lambda/(4\pi R_{Tx}))^2$ and $L_{Rx} = (\lambda/(4\pi R_{Rx}))^2$, where $R_{Tx} = |\Omega_{Tx} - \Omega|$ is the Tx-to-target path length, and R_{Rx} is the distance of the target from the considered receiver, i.e. $R_{Rx} = R_{Rx_{QMS}} = |\Omega_{Rx_{QMS}} - \Omega|$ in the QMS case and $R_{Rx} = R_{Rx_{NFS}} = |\Omega_{Rx_{NFS}} - \Omega|$ in the NFS case, respectively.

Therefore, assuming wide antenna beams (i.e. constant antenna gains within the considered region) and negligible

differences among the sensors heights (i.e. all the sensors lie on the same plane at height H_s), the power ratio in (3) can be simplified as:

$$\Delta S_{NFS/QMS}\big|_{Free\ Space}$$
$$\cong \begin{cases} \left(1 + \dfrac{3D^2}{D^2 + W^2 + 4\Delta H^2}\right)^2 & if\ D \geq \sqrt{2W^2 + 8\Delta H^2} \\ 1 + \dfrac{4D^2}{W^2 + 4\Delta H^2} & if\ D < \sqrt{2W^2 + 8\Delta H^2} \end{cases} \quad (4)$$

where $\Delta H = \max{(H - H_s, H_s)}$.

The adopted metric clearly shows the advantage yield by the NFS configuration in the considered region. In fact, the SNR gain provided by the NFS configuration with respect to the QMS geometry is always greater than unity and approaches unity (0 dB) only for D/W approaching zero (see Figure 2 where the result of eq. (4) is reported for W=80 m and different values of ΔH). In contrast, when the baseline D increases with respect to the width W of the strip region, the result in eq. (4) tends to approximately 4^2=16. In other words, the NFS geometry asymptotically allows a gain of 12 dB against the lowest detectable target position within the region. In addition, notice that the case of a square region ($W = D$) still yields a gain of approximately 6-7 dB and the target height has a limited impact on this comparison.
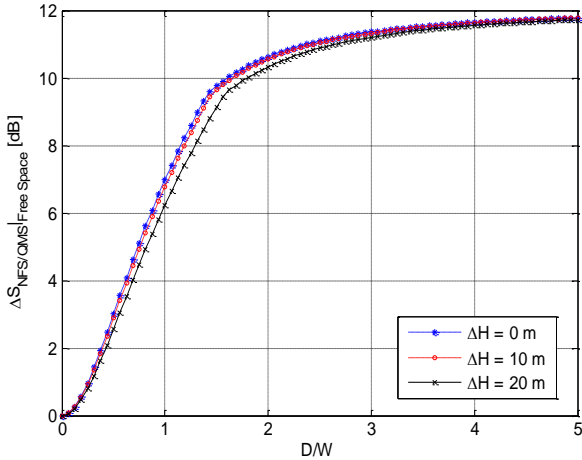

Figure 2. Ratio of the lowest target power levels measured within the surveillance region with the NFS and the QMS sensors configurations assuming a free space propagation model (W=80 m).

B. Two-ray ground reflection model

In order to provide a more realistic evaluation of the improvement allowed by the NFS configuration, in this section we consider a two-ray path (TRP) model to characterize the power level received for a target echo that is affected by multipath formed predominately by a single ground reflected wave [21]. Specifically, by following the approach in [22], the propagation losses in (1) are rewritten as

$$L_{Tx} = \left| \frac{\lambda}{4\pi R_{Tx}} e^{j2\pi \frac{R_{Tx}}{\lambda}} + \Gamma(\alpha_{Tx}) \frac{\lambda}{4\pi R_{Tx'}} e^{j2\pi \frac{R_{Tx'}}{\lambda}} \right|^2 \quad (5)$$

$$L_{Rx} = \left| \frac{\lambda}{4\pi R_{Rx}} e^{j2\pi \frac{R_{Rx}}{\lambda}} + \Gamma(\alpha_{Rx}) \frac{\lambda}{4\pi R_{Rx'}} e^{j2\pi \frac{R_{Rx'}}{\lambda}} \right|^2 \quad (6)$$

where
- $R_{Tx'} = |\mathbf{\Omega}_{Tx'} - \mathbf{\Omega}|$ is the length of the reflected path and can be easily computed by defining the reflected image of the Tx, i.e. $\mathbf{\Omega}_{Tx'} \equiv (-D/2, 0, -H_{Tx})^T$;
- similarly $R_{Rx'} = |\mathbf{\Omega}_{Rx'} - \mathbf{\Omega}|$, being $\mathbf{\Omega}_{Rx'} \equiv (-D/2, 0, -H_{Rx})^T$, is the length of the reflected path from the target to the Rx and can be easily specialized for the QMS or the NFS cases;
- $\Gamma(\alpha_{Tx})$ and $\Gamma(\alpha_{Rx})$ are the complex reflection coefficients. They are functions of the reflected path grazing angle and depend on the ground properties via the dielectric permittivity and the conductivity, on the wave polarization, and on the wavelength.

When the ground projected distances between the target and the Tx (d_{Tx}) or the Rx (d_{Rx}) are much greater than the heights of the sensors and the target, assuming a perfect conducting ground, i.e. $\Gamma = -1$, eqs. (5)-(6) reduce to

$$L_{Tx} \cong \frac{H_{Tx}^2 z^2}{d_{Tx}^4} \quad \& \quad L_{Rx} \cong \frac{H_{Rx}^2 z^2}{d_{Rx}^4} \quad (7)$$

where $d_{Tx} = d_{Rx_{QMS}} = \sqrt{(x + D/2)^2 + y^2}$ and $d_{Rx_{NFS}} = \sqrt{(x - D/2)^2 + y^2}$, so that the loss depends only on the geometry.

Using this approximated TRP model and proceeding as in Section II.A, the power ratio in (3) can be expressed as:

$$\Delta S_{NFS/QMS}\big|_{Approx\ TRP}$$
$$\cong \begin{cases} \left[1 + \dfrac{3D^2}{D^2 + W^2}\right]^4 & if\ D \geq \sqrt{2}W \\ [1 + 4(D/W)^2]^2 & if\ D < \sqrt{2}W \end{cases} \quad (8)$$

As is apparent, even using this propagation model in the considered scenario, the sensitivity ratio is always greater than one and monotonically increases with the aspect ratio D/W of the surveillance region (see Figure 3). Furthermore, compared to the case of a free space propagation model, the result in (8) asymptotically tends to a higher gain (i.e. 24 dB) so that a remarkable improvement is observed for the NFS configuration with respect to the QMS geometry starting from $\frac{D}{W} > 0.5$.

To complete the picture, in Figure 3 we also report the sensitivity ratio in (3) evaluated for the case of a complete TRP model based on eqs. (5)-(6). The reported curves have been obtained by assuming that all the sensors and the target lie on the same plane at height $H_s = 1.25\ m$, the region width is $W = 80\ m$, the carrier frequency is 2.4 GHz and a vertical polarization is assumed. Two different types of surface have been considered (e.g. wet ground and medium dry ground) based on the characteristics extracted from [23]. As expected the result deviates from the approximation based on (7) for low D/W values. Nevertheless the sensitivity ratio still shows the benefits of the NFS geometry that in principle would allow to significantly extend the adopted baseline with respect to a QMS sensors placement thus potentially limiting the number of sensors required to provide a continuous barrier coverage.
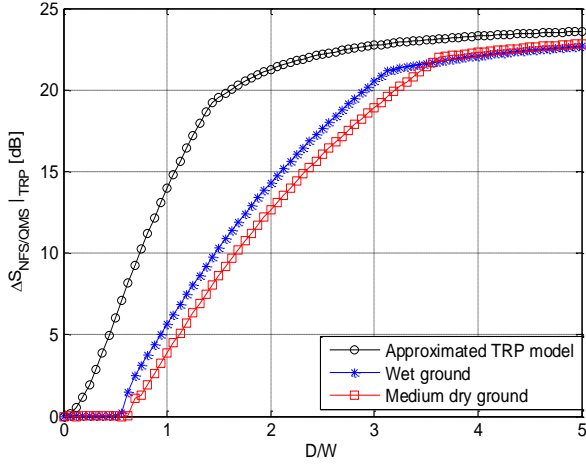
Figure 3. Ratio of the lowest target power levels measured within the surveillance region with the NFS and the QMS sensors configurations assuming a TRP propagation model (W=80 m).

III. EXPERIMENTAL TESTS AND METHODOLOGY ADOPTED

So far we assumed the target to have an isotropic RCS pattern that, besides, was independent of the bistatic angle. Actually, the target RCS depends on the observation geometry, thus both on the bistatic angle and on the target aspect angle.

As well known in the technical literature, using acquisition geometries characterized by high bistatic angles (i.e. close to 180°) typically allows a significant enhancement of the RCS of complex objects [12][24].

If this is confirmed, this characteristic would further favor the NFS configuration in the power budget comparison performed in Section II. However a theoretical analysis of this additional advantage based on a reliable prediction of the target response would be possible only with reference to simple objects. Therefore, in order to characterize realistic situations in this section we carry out an experimental comparison against complex targets.

To this purpose we conducted ad hoc test campaigns. The adopted methodology and experimental setup are described in the next sub-sections.

A. Acquisition geometry and rationale

In this paper we refer to a real world barrier coverage application against vehicular targets. To this purpose, the experimental test reported in the following have been performed in a parking area using different car models as cooperative targets. In such scenario, the exploitation of a WiFi-based passive radar operating in the ISM band represents a suitable solution.

The acquisition geometry is sketched in Figure 4 with reference to the adopted Cartesian coordinate system. The Tx antenna of a commercial WiFi Access Point (AP) was located at $\Omega_{Tx} \equiv (-20\ m, 0\ m, H_s)^T$. Two receiving surveillance antennas were employed. In particular, the first one (Rx_{QMS}) was placed in $\Omega_{Rx_{QMS}} \equiv (-20\ m, 0\ m, 1.6\ m)^T$, in a QMS configuration, while the second one was located in $\Omega_{Rx_{NFS}} \equiv (20\ m, 0\ m, H_s)^T$ in a NFS configuration with a resulting baseline $D = 40$ m. The height H_s of the Tx and Rx$_{NFS}$ has been varied during different tests; the following two configurations

have been used: H_s=1.25 m or H_s=2 m, so that the QMS Rx was a few tenths of centimetres above or below the Tx.

Different car models have been employed as cooperative targets as listed in Table I. The table also reports information about the target size and the number of tests performed against each car model. At each performed test, the driver was asked to move along the y axis from point A to point B in Figure 4 with velocity approximately 4-5 m/s.

It is worth noticing that the target trajectory has been selected so that the target distances to the two receivers is always equal. Moreover, by observing that two identical receivers are employed for the two sensors configurations, we might assume that all the parameters in the corresponding radar equations are identical, except the target RCS. In other words, the theoretical power budget comparison performed in Section II for an ideal isotropic target RCS would provide identical results for the two geometries or, equivalently, $\Delta S_{NFS/QMS} = 1$ along the whole target path.

This allows us to separate the target RCS increase from the changes in the radar equation due to other relevant parameters. Consequently, any difference in the received target power level measured in the experimental data could be reasonably attributed to the different target responses perceived by the two sensors exploiting alternative observation geometries. This analysis is then very useful to investigate the geometry-induced target RCS diversity under real-life conditions.

Incidentally, we also observe that the considered geometry (i.e. target crossing the Tx-Rx baseline at the mid-point) could be regarded as a worst case condition for the NFS configuration as the received signal power is expected to be minimal according to a forward scatter mechanism [12][13].
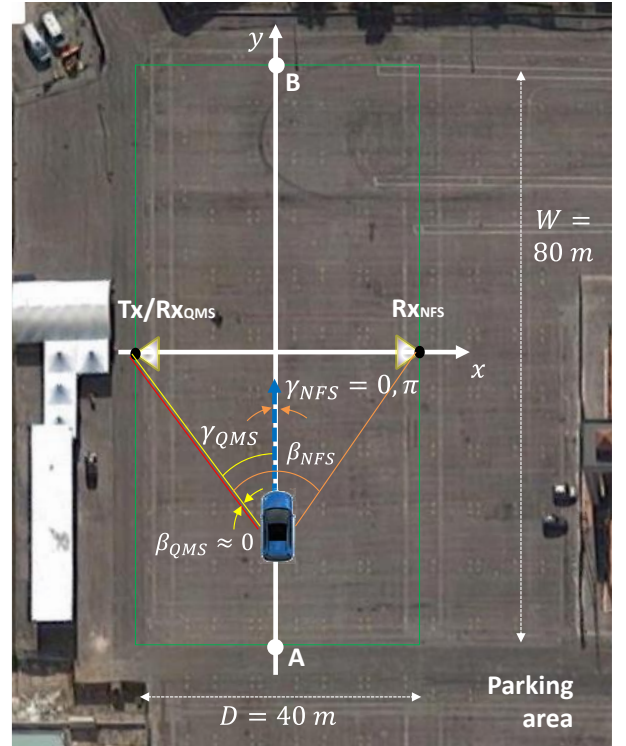

Figure 4. Sketch of the acquisition geometry and experimental setup.

TABLE I – CAR MODELS EMPLOYED IN THE REPORTED EXPERIMENTAL TESTS.

Car model	Picture	Dimensions [m]	Number of tests
Peugeot 107		3.43 x 1.63 x 1.47	4
Fiat Punto Evo		4.065 x 1.690 x 1.49	4
Citroen C3		3.941 x 1.728 x 1.524	3
Volkswagen Polo		3.715 x 1.655 x 1.420	4

Specifically, when the QMS receiver is used, the target RCS only varies according to the different aspect angles γ_{QMS} experienced along the target path ($\beta_{QMS}\sim0$ at any target position). In the considered geometry, γ_{QMS} spans the interval [26.6°, 153.4°]. In particular fast variations could be expected for a complex target since target backscatter is largely affected by its shape and material.

In the NFS case, for the considered tests, the aspect angle γ_{NFS} can only take values equal to 0° or 180° (we recall that it is defined as the angle between the major axis of the target and the radar LOS, the latter being the direction of the bistatic angle bisector). However, the target RCS might still vary with the bistatic angle β_{NFS} that depends on the target current position $\Omega \equiv (x, y, z)^T$ within the region:

$$\beta_{NFS}(\Omega) = acos\left\{\frac{\Omega_{Tx} - \Omega}{|\Omega_{Tx} - \Omega|} \cdot \frac{\Omega_{Rx_{NFS}} - \Omega}{|\Omega_{Rx_{NFS}} - \Omega|}\right\} \qquad (9)$$

In the considered test geometry, the bistatic angle takes its minimum value ($\beta_{NFS} = 53.1°$) at the outer points (A-B) of the target trajectory whereas it reaches 180° as the target traverses the baseline.

When the target is in the proximity of the baseline, by definition, the Tx-Rx pair constitutes a forward scatter radar in the strictest sense [12][13][24]. Under such conditions the target response does not experience phase fluctuations and significantly enhances as the result of the coherent summation of all scattering components of the target at the observation point. The higher the operating frequency the greater the forward scatter signal strength for the same Tx power, while the angular extent of the region of high forward scatter RCS reduces.

Just outside this region, the Tx-Rx pair system operates as a bistatic radar with very high bistatic angles. We refer to this region as the near forward scatter region (see Figure 5) and we roughly define it as the region contained within the ellipsoid having as foci the Tx and the NFS Rx and major axis equal to half the bistatic range resolution c/B (being c the light speed and B the signal bandwidth). Basically target echoes originating from that region show a maximum delay of $1/(2B)$ with respect to the signal from the Tx so that they directly compete with such

direct signal even after a range compression stage. In our experiment, as the bistatic range resolution is approximately 27.3 m, the smallest bistatic angle experienced along the target trajectory confined within this region is $\beta_{NFS} = 96.4°$ at $y = \pm17.9$ m. Within this region, it is difficult to predict how far the three-dimensional nature of the object affects the bistatic scattering pattern. However there are reasons to believe that the resulting bistatic radar can still benefit from the enhanced RCS produced by the forward scatter mechanism [24].

Apparently, the tests performed allow to experimentally verify the above considerations with particular reference to the considered application, i.e. for vehicular targets at S band.

B. WiFi-based passive sensors setup and signal processing scheme

In this paper we employed the WiFi-based passive radar sensor developed at Sapienza University of Rome [5]. In the reported acquisition campaign, a commercial WiFi AP was used as Tx of opportunity. The router was configured to transmit in channel 6 of the WiFi band (2437 MHz). It was set up to emit a regular Beacon signal exploiting a DSSS modulation at 3 ms intervals. The AP antenna output was connected to the Tx antenna while a directional coupler was used to send a −20 dB copy of the transmitted signal to the first receiving channel of a quad-channel receiving system with the aim of collecting the reference signal (see sketch in Figure 6). In fact the illuminator of opportunity is assumed to be partially cooperative thus providing direct access to the transmitted signal. Other two identical receiving channels of the available system were used to acquire simultaneously and synchronously the signals received by QMS and NFS Rx antennas. All the adopted antennas are commercial WiFi panel antennas and are characterized by a 12 dBi gain, a front-to-back ratio of 15 dB and beamwidths equal to 80° and 23° on the horizontal and vertical plane, respectively. Moreover, for a fair comparison, we employed cables of the same length in order to have comparable losses in both QMS and NFS configurations.

After a fully coherent base-band down-conversion stage, continuous and simultaneous acquisitions are performed at the different receiving channels: the signals collected are sampled at 22 MHz and stored for off-line processing. Acquisitions of duration between 15 s and 20 s are made available for the different tests performed, accounting for the whole target trajectory along the selected path.
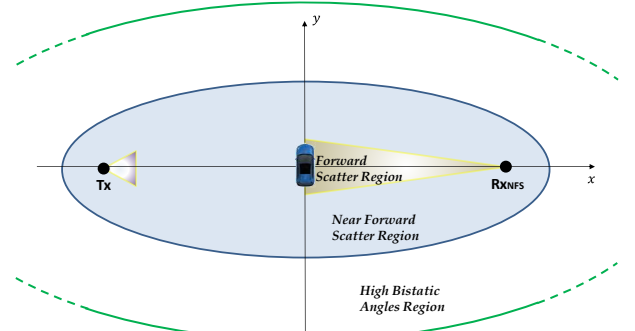

Figure 5. Regions definition for the NFS receiver along the target trajectory.

It is worth mentioning that, aiming to an accurate comparison of the power received from the target, each single component of the receiving system has been appropriately selected and optimized in order to guarantee a very high SNR. These choices include the use of directional antennas, low noise amplifiers with high gain and the highest allowed power level for the AP. In such conditions, the target detection capability of both the considered configurations is expected to be extremely high (i.e. detection rate close to 100%) and not very representative of a practical condition. Therefore when a comparison is sough in term of achievable detection rate, a proper Gaussian noise contribution is injected in the available acquisition to simulate a typical noisy condition.

For the purpose of our analysis, for all the performed tests, the signals collected at the QMS and the NFS channels separately underwent the WiFi-based passive radar processing scheme for target detection depicted in Figure 6 and reported by the same authors in [5][7][9]. In such processing scheme, disturbance cancellation represents an essential stage. This operates against the range-compressed outputs obtained by cross-correlating the surveillance and the reference signals on a pulse basis.

Notice that a pre-conditioned reference signal is exploited aiming at improving the sidelobes level in the resulting mismatched ambiguity function in the range dimension. The removal of undesired contribution (i.e. direct signal from the Tx and its multipath replicas) is performed in the following using the sliding version of the Extensive Cancellation Algorithm (ECA-S), [25]. Its parameters have been selected to operate over a range extent of 500 m (i.e. 36 taps $@f_s = 22$MHz) with a bath duration equal to 100 ms whereas the filter update rate is set to be equal to the AP beacon emission rate. These values were verified to yield remarkable cancellation performance against the varying characteristics of the environment while preserving slowly moving target echoes.

After the above stages, target detection is sought by evaluating the bistatic range-velocity map over the desired coherent processing interval (CPI). A CPI of 0.1 s is used in the following analyses. The selected CPI length yields a Doppler resolution cell that is expected to include the instantaneous Doppler bandwidth of the employed targets along their path so that they appear as point-like; therefore the peak value measured on the resulting range-velocity map represents a characteristic of the target as a whole and intrinsically includes the interference among its scatterers. In other words, the peak value measured at the target range-velocity location is a measure of its SNR; therefore, based on the selected symmetrical test geometry and the adopted receiver setup, the comparison of the results obtained with the QMS and the NFS sensors provides indications about the target RCS diversity under the two configurations.

Finally, a Cell-Average constant false alarm rate (CA-CFAR) threshold is applied on the obtained map to automatically detect targets over the bistatic range/velocity plane with a nominal probability of false alarm P_{fa}. Comparing the achievable detection rate will provide immediate understanding of how the above RCS diversity affects the detection capability of the systems.

IV. RESULTS AGAINST LIVE DATA

A. Comparison of the estimated SNR

By processing consecutive 0.1 s portions of the available signals, a sequence of range-velocity maps (frames) is obtained covering the whole acquisition.

As an example, Figure 7 shows the range-velocity maps obtained at the same frame with the QMS and the NFS sensors, for two different tests employing two different cars. All the reported maps have been normalized to thermal noise power level (which is identical at the two receivers) so that the value at each map location represents the estimated SNR.

Specifically, Figure 7 refers to the test with the Peugeot 107 and the selected frame corresponds to the case of the target approaching the baseline. Thanks to the symmetry of the target
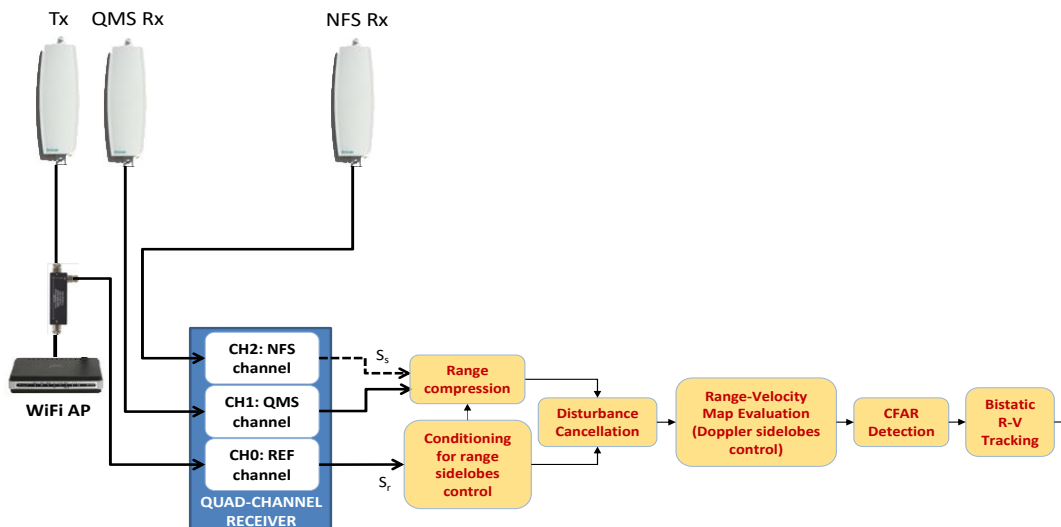

Figure 6. WiFi-based passive radar setup and signal processing scheme.

trajectory with respect to the two considered sensors configurations (QMS and NFS), the target instantaneously occupies the same bistatic range-velocity location on the resulting maps. In particular at the selected frame the target appears as a strong peak at 43 m and 3 m/s. In addition, further peaks are also visible caused by the double bounce reflection of the target echo over the metallic structures delimiting the parking area (see Figure 4). Notice that, for both the QMS and the NFS geometries, the target is responsible for the highest peak in the map and this is characterized by SNR values higher than 45 dB.

As previously mentioned this is a condition sought in order to perform a reliable comparison of the results obtained with the two sensors. Anyway the peak value registered for the NFS sensor (55.1 dB) is higher than that observed with the QMS receiver (48.2 dB): a gain of about 7 dB is measured in this case.
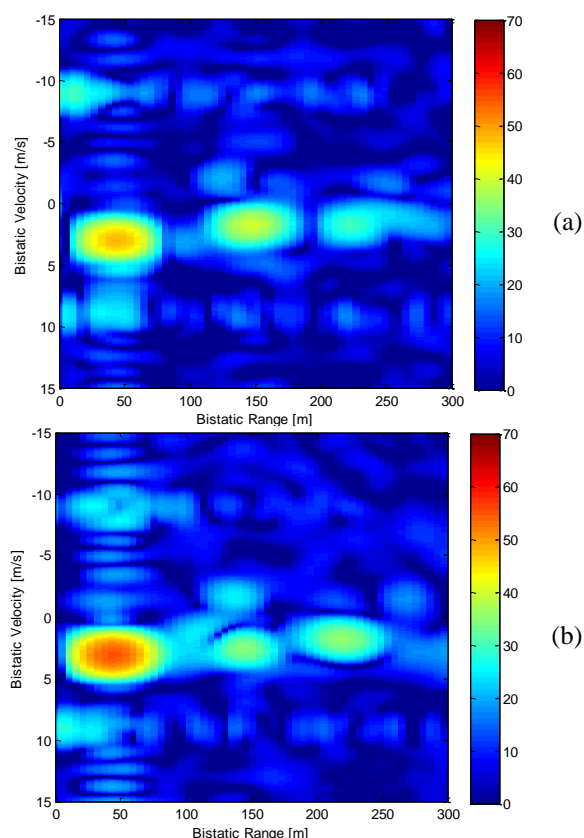

Figure 7. Range-Velocity maps for a test with the Peugeot 107 ($H_s = 1.25\ m$). (a) QMS receiver; (b) NFS receiver.

By collecting the peak values extracted for the target at each frame, the estimated SNR is obtained along the target trajectory, i.e. along the acquisition time, with a sampling rate of 10 frames per second. Typical results have been reported in Figure 8 for four different tests employing the four car models considered in the campaign. In each figure, the estimated SNR curve is reported for both the QMS (blue curve) and the NFS (magenta curve) sensors configurations. Missing values refer to frames in which the target echo was very weak so that it could not be clearly recognized (i.e. detected) as a peak in the resulting range-velocity map.

Based on a rough estimate of the target velocity, the SNR curves are reported as a function of the target position along its trajectory. In each figure, different path portions are identified corresponding to the target passing through the different regions defined in Figure 5. Specifically, red vertical lines are used to separate the near forward scatter region from the region characterized by high bistatic angles. The borders of the strict forward scatter region are indicated with black vertical lines. The latter is identified based on the output of the range compression stage in Figure 6; the obtained curve is also reported in Figure 8 for direct comparison (labeled as 'target signature'). Notice that, when the target crosses the baseline (i.e. $y \sim 0$), it creates an area of significant signal reduction at the NFS Rx. In fact the signal reflected by the target has a low to zero Doppler content and destructively interferes with the direct signal travelling from the Tx antenna to form a shadow directly behind the car. In [20] we have shown that the shape of the signal notch is characteristic of the considered car model so that this target signature could in principle allow vehicles classification. To this purpose, the output of the range compression stage could be simply exploited without requiring the advanced processing stages in Figure 6. Actually, the successive processing stages, particularly the disturbance cancellation, could be detrimental to the target signature preservation as the signal contributions around the zero Doppler are significantly modified.

However, in this paper the focus is on the detection of targets crossing a given barrier with some breadth; therefore it is of high interest the possibility to provide an early warning capability against the intruder before it reaches the baseline, namely when it is moving in the near forward scatter area or even in the area of high bistatic angles. Under these conditions, a disturbance cancellation stage is strictly required in order to enhance the target detection performance. Moreover, we observe that the presence of the target in the forward scatter area can be easily detected by detecting the signal reduction discussed previously.

For the reasons above and in order to perform a fair comparison between the NFS and the QMS configurations, we exclude the forward scatter area from the following analysis.

Coming back to Figure 8, we observe that at both the NFS and the QMS Rx, the estimated SNR gets lower as the target moves away from the baseline. However the measured SNR is usually higher at the NFS Rx (see the magenta curves) with respect to the QMS Rx (see the blue curves), both in the near forward scatter region and in the high-bistatic angles region. With some car models the advantage is more apparent since the NFS curve is nearly always above the corresponding QMS result. This is for example the case of the Peugeot 107 (see Figure 8(a)) for which the SNR gain exceeds 15 dB at specific points (e.g. abscissae y=10 m and y=-7 m). Anyway, with all the considered car models, the NFS configuration provides a SNR gain exceeding 10 dB at specific target positions (e.g. y=-13 m in Figure 8(b), y=12 m in Figure 8(c), and y=-10 m in Figure 8(d)).

In addition, the SNR curve estimated at the NFS Rx has a much smoother trend along the target path; this in turn shows
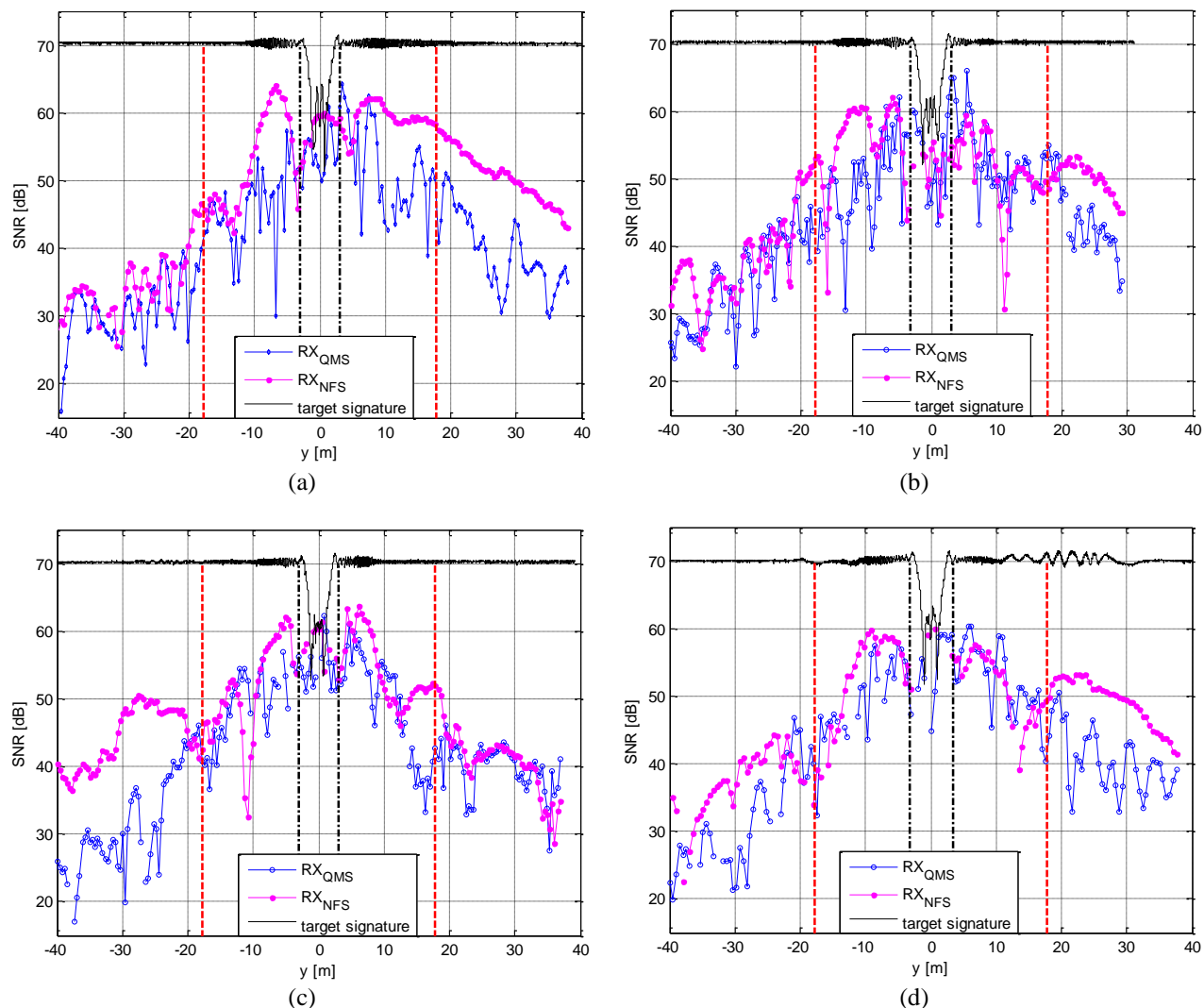
Figure 8. Comparison of the estimated SNR vs target position along the y axis for different tests employing different vehicles: (a) Peugeot 107; (b) Fiat Punto Evo; (c) Citroen C3; (d) Volkswagen Polo.

that the target observed under this geometry yields a RCS pattern that is highly correlated in space, namely small variations are observed among neighboring target positions. In contrast the RCS pattern of the same target under the QMS configuration is extremely variable along the target path and abruptly changes as the car occupies successive positions.

This is quite typical of a complex target backscattering as it is largely affected by the target shape and material that determine the individual scatterers contributions which differently combine at the Rx when varying the aspect angle.The superior stability allowed by the NFS geometry is confirmed in Figure 9 where the SNR curves are shown for the same car model (the Peugeot 107) as obtained at the four available tests employing this car.

Specifically Figure 9(a) refers to the tests with the Tx and the NFS Rx antennas mounted at $H_s = 1.25\, m$, while Figure 9(b) is for the cases of $H_s = 2\, m$. As is apparent the target yields very similar SNR curves at different tests employing the same

geometry and this shows that the reported analysis is quite reliable.

Notice that the stability is more evident with the NFS geometry, especially when using antennas height H_s comparable with the target vertical size (see Figure 9(a)) since the considered Rx antenna is likely to be still affected by the shadowing effect produced by the forward scattering mechanism as the target moves along its path. When raising the antennas, the bistatic angle consequently reduces due to the non-zero grazing angle so that the advantage of an enhanced and more stable RCS gets smaller. This can be observed by comparing the results of the NFS configuration in Figure 9(a) and Figure 9(b). Nevertheless, the higher stability and the enhancement of the SNR values measured at the NFS Rx with respect to the QMS Rx is apparent even in Figure 9(b), especially in the near forward scatter area.
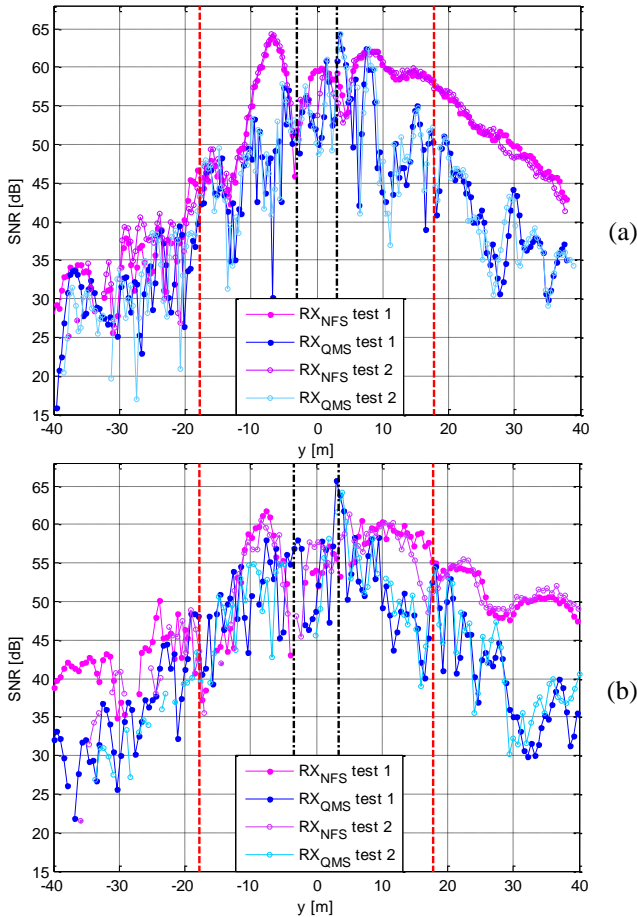
(a)

(b)

Figure 9. Comparison of the estimated SNR curves obtained at different tests for the Peugeot 107: (a) results obtained at two tests using $H_s = 1.25\ m$; (b) results obtained at two tests using $H_s = 2\ m$.

It is due to mention that the estimated SNR is far from being ideally related to the target radiating characteristics only. In fact it might be affected by several factors that are independent of the target as listed below:

(i) reflections from the ground and from stationary objects surrounding the parking area (i.e. multipath). Notice that, after range compression, the multipath originated from buildings and ostacles are well separated from the target echo in the range dimension (see double bounce effects in Figure 7). In contrast multipath from the ground directly competes with the target echo yielding constructive or destructive effects depending on the instantaneous geometry. However, in this regard we observe that the geometry adopted for the QMS and the NFS sensors is almost identical so that they are expected to be similarly affected by ground reflections.

(ii) The SNR measurements could be affected by the cancellation stage especially at low Doppler values. As the cancellation algorithm is able to adapt to the observed disturbance scenario, the resulting filter intrinsically yields slightly different cancellation notches that differently influences the target echo. In this regard we notice that in the QMS configuration, the target echo has a relative delay corresponding to at least 1.5 range cells (>40 m) with respect to the direct signal, which represents

the most powerful disturbance contribution. In contrast, when employing a NFS geometry, the target crossing the baseline appears at exactly the same range cell of the direct signal from the Tx; therefore it is reasonable to assume that its echo will undergo a much deeper cancellation notch around the zero Doppler. However the parameters selected for the adopted ECA-S algorithm allow to synthesize a cancellation notch with a -4dB width narrower than 16 Hz (or equivalently 2 m/s) [25] which is likely to be mostly contained in the forward scatter area that has been excluded from the analysis.

Based on the considerations above it is more correct to state that the obtained SNR values depend on the target RCS pattern and on its interactions with the scene. Therefore we cannot exploit the available data to directly estimate the target RCS as this would require dedicated tests in anechoic chamber. We rather use the performed tests to compare the QMS and the NFS configurations aiming at highlighting their differences in a practical scenario. This is indeed the comparison that is extremely valuable for the real application.

B. Comparison of the detection results

The advantage yield by the NFS configuration in term of target SNR might provide a significant improvement in detection capability compared to the monostatic or pseudo-monostatic sensors configuration. However, due to the very high SNR values used for the experiments (see Figure 8), the collected data set cannot be directly used to demonstrate this improvement since both NFS and QMS sensors have asymptotic detection performance. In order to emulate a practical condition, zero-mean complex Gaussian white noise is deliberately injected in the recorded data with power level ΔP_n. Therefore the actual noise power level is boosted to $P'_n = P_n + \Delta P_n$ (being P_n the receiver original noise power level) so as to produce a SNR degradation equal to $\Delta SNR_{dB} = 10\ log_{10}(1 + \frac{\Delta P_n}{P_n})$ dB.

At each test, for a given noise power level, target detection is performed frame by frame on the bistatic range-velocity map by resorting to a CA-CFAR threshold with a probability of false alarm P_{fa} equal to 10^{-4}. Figure 10 reports an example of the detection results obtained for the test considered in Figure 8(a) when the original SNR is degraded by 25 dB.

In particular Figure 10(a) is for the QMS Rx while Figure 10(b) shows the results of the NFS sensor. In each case, the raw detection results provided by the passive radar sensor are reported as 'x' markers. A light grey line is used for the available ground-truth and indication is provided in Figure 10(b) of the different bistatic angles regions.

As expected, the target observed under the two geometries describes identical trajectories on the bistatic range/velocity plane. However, the number of correct detections significantly varies with the two sensors configurations with a remarkable advantage of the NFS geometry. In addition, we observe that the range/velocity measurements provided by the NFS sensor are much more accurate than in the QMS case where high

fluctuations can be noticed around the true target trajectory.

A similar analysis has been repeated for different cars. By summing up the number of correct detections obtained along the target trajectory (or its portions) at all the available tests employing the same car model, we obtain the results listed in Table II. Specifically the table reports, for each employed car:
- the number of available frames, namely the maximum number of potential detections, compared to
- the number of detections yield by the QMS sensor, and
- the number of detections yield by the NFS sensor.

The results are provided by distinguishing between the near forward scatter area and the region of high bistatic angles; the last group of columns report the overall results along the target path (with the exclusion of the strict forward scatter region).
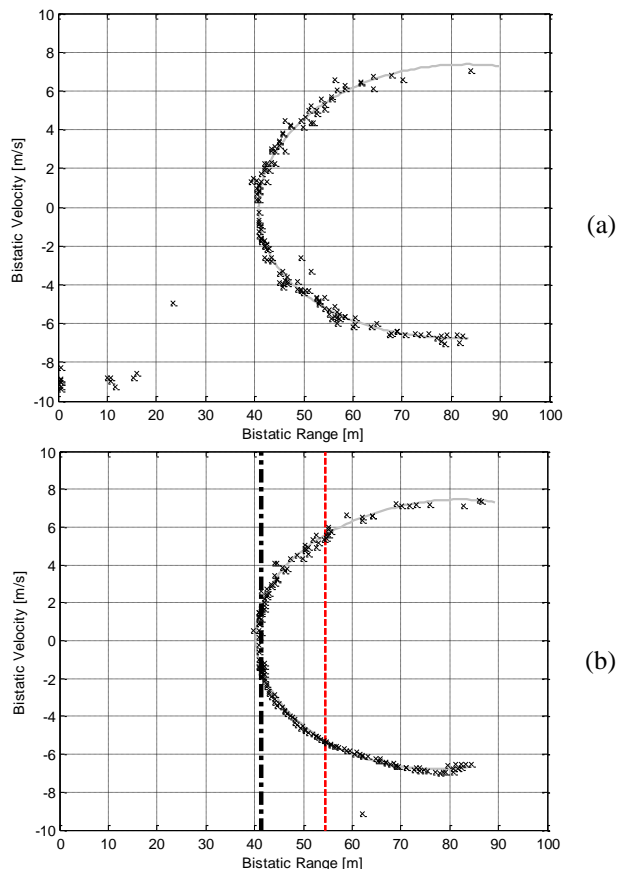

Figure 10. Detection results for the test against the Pegeout 107 with 25 dB SNR degradation and $P_{fa} = 10^{-4}$ for (a) the QMS sensors configuration; (b) the NFS sensors configuration.

TABLE II – DETECTION RESULTS FOR VARIOUS CAR MODELS AVERAGED OVER THE AVAILABLE TESTS WITH 25 DB SNR DEGRADATION AND $P_{fa} = 10^{-4}$.

Car model	Near Forward Scatter Region			High Bistatic Angles Region			Whole target trajectory		
	# of frames	Det. QMS	Det. NFS	# of frames	Det. QMS	Det. NFS	# of frames	Det. QMS	Det. NFS
Peugeot 107	311	282	295	297	114	213	608	396	508
Fiat Punto Evo	346	317	336	293	127	163	639	444	499
Citroen C3	252	223	241	284	139	214	536	362	455
Volkswagen Polo	250	213	232	316	116	210	566	329	442

For all the considered car models, the NFS sensor yield a remarkable increase in correct detections with respect to the QMS configuration.

The advantage is more apparent in the region of high bistatic angles as this is characterized by generally lower SNR values due to the increase of the target distance from both the sensors. In contrast, despite the SNR degradation, the near forward scatter area is more representative of an asymptotic detection performance region so that the improvement provided by the NFS sensor appears to be smoothed. Nevertheless, many additional detections are obtained thus increasing the final detection rate.

This is also quite apparent in Figure 11 which provides an extensive analysis. Specifically, we repeated the calculations above by varying the additional noise power level so as to produce increasing SNR degradations (from 0 dB to 35 dB) and the P_{fa} value used to set the threshold. Using all the available tests (even employing different cars) and evaluating the ratio between the total number of correct detections and the global number of frames, we obtained an estimate of the detection rate for the QMS and the NFS sensors. The results are reported in Figure 11(a) for the near forward region only, in Figure 11(b) for the high bistatic angles region only, and in Figure 11(c) when averaged along the whole target path.

Clearly the detection performance in the region of high bistatic angles rapidly gets worse as the imposed SNR degradation increases and this effect is even more evident for the lower P_{fa} value (see Figure 11(b)). A similar trend is observed also in the near forward scatter region (Figure 11(a)) when further increasing the additional noise power level. In any case the NFS sensor yields a sensibly improved detection capability as the resulting detection rate along the whole target trajectory is well above that provided by the QMS sensor.

V. STRATEGIES TO EXPLOIT THE BENEFITS OF THE NFS SENSORS CONFIGURATION

With reference to the considered application, aiming at a continuous barrier coverage, the peculiar characteristics and the performance improvement provided by the NFS sensors configuration could be in principle exploited to reduce the number of sensors required to protect a given barrier or, alternatively, they could be traded for a reduced implementation costs.

Following the latter approach, we show an example of the possible reduction of the signal processing complexity and, in turn, the simplification of the dedicated HW components. So far we assumed that the data collected by the QMS and the NFS sensors undergo the same signal processing steps adopting the same set of relevant parameters.

In the following we show that the NFS sensors allows a sensible reduction of the processing complexity by acting on:
- the range extent of the bistatic range/velocity map, and
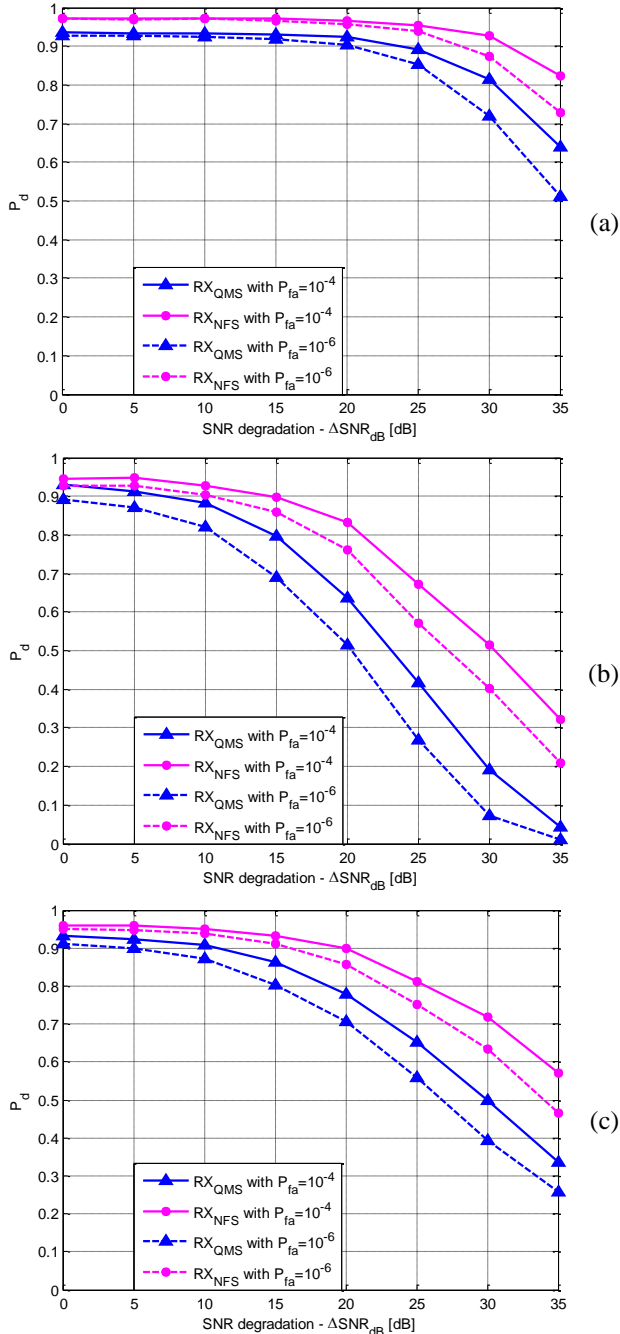- the number of taps exploited by the cancellation filter.

(a)

(b)

(c)

Figure 11. Comparison between the QMS and the NFS sensors configuration in term of detection rates vs SNR degradation with different values of P_{fa} for (a) the near forward region only; (b) the high bistatic angles region only; (c) along the whole target path.

A. Reduction of the range extent of the bistatic range/velocity map

Whilst in Section IV the analysis has been performed by evaluating range/velocity maps with the same dimensions, aiming at the coverage of a barrier with some breath as defined in Figure 1, the NFS configuration potentially allows a reduction of the bistatic range extent to be considered.

In fact the bistatic range extent of the surveyed region is defined as $\Delta R_B = R_{Bmax} - R_{Bmin}$, where R_{Bmax} and R_{Bmin} are the maximum and the minimum bistatic ranges associated

to a target belonging to that region. For the QMS and the NFS sensors placement defined in Figure 1, the bistatic range of a target in $\boldsymbol{\Omega} \equiv (x, y, z)^T$ can be readily written as:

$$R_{B_{QMS}} = R_{Tx} + R_{Rx_{QMS}} \tag{10}$$

$$R_{B_{NFS}} = R_{Tx} + R_{Rx_{NFS}} \tag{11}$$

A direct comparison in term of required bistatic range extent between QMS and NFS geometries is provided by the ratio:

$$\Delta E_{QMS/NFS} = \frac{\Delta R_{B_{QMS}}}{\Delta R_{B_{NFS}}} = \frac{\max_{\boldsymbol{\Omega} \in \Sigma}\{R_{B_{QMS}}\} - \min_{\boldsymbol{\Omega} \in \Sigma}\{R_{B_{QMS}}\}}{\max_{\boldsymbol{\Omega} \in \Sigma}\{R_{B_{NFS}}\} - \min_{\boldsymbol{\Omega} \in \Sigma}\{R_{B_{NFS}}\}} \tag{12}$$

Using the same hypotheses adopted in Section II, the maximization/minimization of the various terms in (12) yields:

$$QMS: \begin{cases} \min_{\boldsymbol{\Omega} \in \Sigma}\{R_{B_{QMS}}\} = 0 \quad at \; \boldsymbol{\Omega} \equiv \left(0, -\frac{D}{2}, H_s\right) \\[2mm] \max_{\boldsymbol{\Omega} \in \Sigma}\{R_{B_{QMS}}\} = 2\sqrt{D^2 + \frac{W^2}{4} + \Delta H^2} \\[2mm] \qquad at \; \boldsymbol{\Omega} \equiv (D/2, \pm W/2, H_s + \Delta H) \end{cases} \tag{13}$$

$$NFS: \begin{cases} \min_{\boldsymbol{\Omega} \in \Sigma}\{R_{B_{NFS}}\} = D \quad at \; \boldsymbol{\Omega} \equiv (x, 0, H_s) \\[2mm] \max_{\boldsymbol{\Omega} \in \Sigma}\{R_{B_{NFS}}\} = \sqrt{\frac{W^2}{4} + \Delta H^2} + \sqrt{D^2 + \frac{W^2}{4} + \Delta H^2} \\[2mm] \qquad at \; \boldsymbol{\Omega} \equiv (\pm D/2, \pm W/2, H_s + \Delta H) \end{cases} \tag{14}$$

Consequently the ratio in (12) becomes:

$$\Delta E_{QMS/NFS} = \frac{2\sqrt{\dfrac{4D^2}{W^2 + 4\Delta H^2} + 1}}{1 + \sqrt{\dfrac{4D^2}{W^2 + 4\Delta H^2} + 1} - \sqrt{\dfrac{4D^2}{W^2 + 4\Delta H^2}}} \tag{15}$$

The result of eq. (15) is reported in Figure 12 for W=80 m and different values of ΔH. As is apparent the ratio $\Delta E_{QMS/NFS}$ is always greater than one and approaches unity only for D/W approaching zero. Basically, the two configurations become comparable when $W \gg D$. In contrast, $\Delta E_{QMS/NFS}$ linearly increases with the ratio D/W.
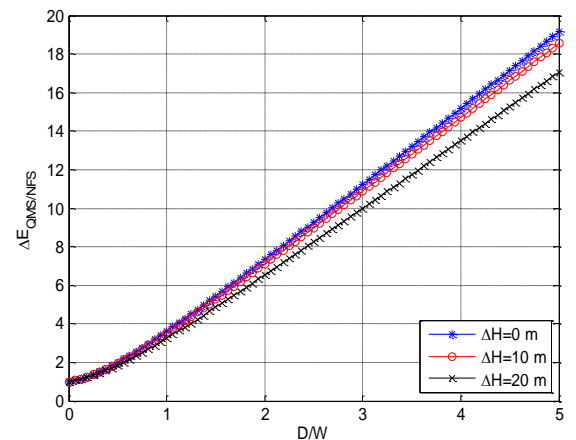

Figure 12. Ratio of the bistatic range extents required to include the whole surveillance region with the NFS and the QMS configurations (W=80 m).

In other words, the NFS geometry always allows a reduction of the bistatic range extent required by the processing in order to cover the whole surveillance region. As an example, in the case $D = W$, the NFS sensor needs to evaluate bistatic maps with a range extent approximately 3.5 times smaller than the QMS sensor and the advantage becomes higher when the baseline D increases.

Such reduction is expected to yield a corresponding simplification of the required computations at different signal processing stages. In particular, assuming that the signal processing flow is implemented as described in Section 3.B (see Figure 6), the disturbance cancellation and the range-velocity map evaluation are obtained based on the results of the (pulse-by-pulse) cross-correlation between the reference and the surveillance signal and the corresponding reference signal auto-correlation.

Such results should be evaluated on a range extent equal to the maximum bistatic range to be covered (as long as the number of cancellation taps is equal or smaller than the number of bistatic range cells). Obviously, reducing the required range extent yields a corresponding reduction in term of storage requirements. In addition, the evaluation of a limited number of range bins allows a corresponding reduction of the computational load. In this regard, the following considerations apply depending on the method adopted to evaluate the required outputs:

- if conventional FFTs are exploited to evaluate the cross- and auto-correlations, the computational load would be independent of the map range dimension. Nevertheless the synthesis of the Doppler dimension via FFT over the slow-time (i.e. across the results obtained at successive pulses) would require a number of complex operations proportional to the number of range cells included in the map.
- When a FPGA-based processing is employed or when the number of range cells becomes extremely small (2 or 3 cells), the direct evaluation of the required lags of cross- and auto-correlations might be the most efficient solution. In such cases, the advantage of a limited bistatic range extent could be even more apparent.

Finally, a further computational load saving is expected at the detection stage, namely for CFAR threshold evaluation and application on the range/velocity map. In this case, a reduction of the map range extent yields a linearly proportional reduction of the number of operations.

For illustrative purposes, we evaluate the computational load required by the processing stages discussed above as a function of the number of range cells N_R with reference to the application considered in this paper based on the parasitic exploitation of WiFi transmissions. Specifically, by taking into account the considerations above, the efficient evaluation of the bistatic range-velocity map and the successive application of a CA-CFAR scheme for target detection require

$$C_1(N_R) = B \left\{ \min[N_R(8N-2), 15N \log_2 N + 6N] \right.$$
$$\left. + 5N_R \log_2 B \right\} + N_R N_V(M_C + 3) \quad (16)$$

FLOPs (FLoating-point Operations; here we assume that a complex add involves 2 FLOPs and a complex multiplication involves 6 FLOPs).

The parameters appearing in (16) are defined as follows: B is the number of pulses (e.g. beacons) included in the CPI and, for the sake of simplicity, we assume that they all have equal length of N samples; N_V is the number of velocity bins included in the map and depends on the maximum observed velocity for the considered targets; M_C is the number of secondary cells adopted by the CA-CFAR scheme to estimate the disturbance power level.

As is apparent, the required number of FLOPs linearly increase with the number of range bins N_R. Therefore, the reduction of this number allowed by the NFS sensor results in a corresponding computational load reduction with respect to the QMS sensor operating in the same scenario. In practice, for limited N_R values (i.e. reasonably small range extents, approximately smaller than 350 m in our experimental set-up), the constant of proportionality in (16) might be very high. In fact such constant becomes equal to $B[8N - 2 + 5\log_2 B + N_V(M_C + 3)]$ so that a large number of FLOPs can actually be saved when using the NFS sensor. As a reference, Figure 13 reports the number of FLOPS evaluated using (16) as a function of the number of range cells N_R (see the blue discontinuous curve). The other parameters were set to be coincident with those adopted in the considered experiment. As in our case D/W=0.5, the number of range cells N_R required by the processing of the NFS sensor is just halved with respect to the QMS configuration (see Figure 12). This obviously yields a reduction of the number of FLOPs only by a factor of 2 but, with the considered parameters, this corresponds to a number of FLOPs saved in the order of 10^8.

Such computational load saving in the NFS sensor is due to its capability to enclose the region of interest within a reduced number of range cells and does not imply any performance degradation.

A further reduction of the processing scheme complexity could be achieved by varying the number of cancellation taps and accepting a limited detection performance loss, as shown in the next sub-section.
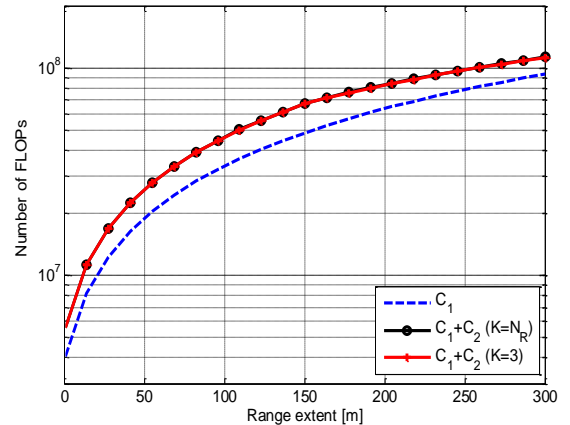

Figure 13. Number of FLOPs required by the WiFi-based passive radar processing scheme as a function of the range extent of the bistatic range-velocity map.

B. Reduction of the cancellation filter taps

Based on the performance comparison reported in Section IV, the NFS sensor configuration employed in the conducted experimental tests always allows an enhancement of the vehicular target detection capability with respect to the QMS sensor geometry. In this sub-section we show that such improvement could be partly traded for a reduction in the cancellation filter complexity.

To this purpose, Figure 14 reports the estimated detection rate obtained with the NFS and the QMS as a function of the number of taps K adopted by the ECA-S cancellation algorithm [25]. Figure 14(a) refers to the near forward scatter region while Figure 14(b) accounts for the whole target trajectory. The results have been averaged on all the available experimental tests with a SNR degradation of 25 dB and both $P_{fa} = 10^{-4}$ or $P_{fa} = 10^{-6}$. As is apparent, with the NFS configuration, a few taps are sufficient to reach the asymptotic performance; particularly 1-2 taps are enough in the near forward scatter region whereas using 3 taps almost guarantees asymptotic performance along the whole target path.
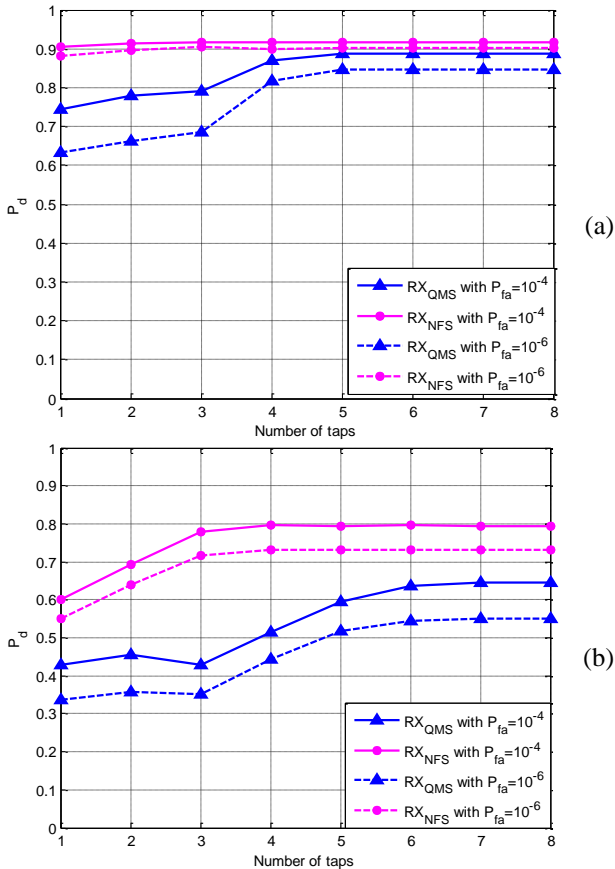

(a)

(b)

Figure 14. Comparison between the QMS and the NFS sensors configuration in term of detection rates vs number of taps with different values of Pfa and ΔSNR_{dB}=25 dB for (a) near forward region only; (b) the whole target path.

In contrast, the QMS sensor requires at least 4 taps in the near forward scatter region and about 6 taps to guarantee a performance convergence along the whole target trajectory.

The advantage of the NFS is due both to:

- the enhancement of the power level received from the target that is effectively exploited also against disturbance residuals resulting from a reduction in the number of taps, and
- the characteristic geometry adopted which implies that the target echo mostly competes with the direct signal from the Tx and multipath from the first range cells; therefore, using a few taps provides an effective removal of the highest contributions limiting the target detection. Notice that even one single tap could be sufficient in the near forward scatter region where the target echo detection is mostly affected by the signal travelling from the Tx. In addition we observe that, in this case, the achievable detection rate is still higher than the asymptotic value provided by the QMS sensor.

The number of taps affects the complexity of the cancellation stage as it sets the dimension of the matrix to be estimated and inverted, as well as the dimension of the filter to be evaluated and applied. Therefore, the potential reduction of this number might enable a corresponding reduction in the computational load of this processing stage.

To quantify this reduction, we consider the efficient implementation of the ECA-S proposed in [25] and evaluate the additional number of FLOPs required by the disturbance cancellation stage as a function of the number of range cells N_R and the number of taps K:

$$C_2(N_R, K) = B \left\{ \min\left[N_R(3N - 1), \frac{5}{2}N \log_2 N + 3N \right] \right.$$
$$+ 4B_A K + 16K^2 + N_R \qquad (17)$$
$$\left. + \min[N_R(8K - 1), 10N \log_2 N + 6N] \right\}$$

where B_A is the number of consecutive pulses used for adaptive estimation of cancellation filter coefficients.

The total number of FLOPS obtained by summing the contributions C_1 and C_2 provided in (16) and (17), respectively, is reported in Figure 13 for comparison. The results are reported as a function of the number of range cells N_R for different number of taps K. In particular both the case of $K = N_R$ and $K = 3$ are shown which provide largely comparable results.

As is apparent by comparing the C_1 contribution (discontinuous curve) with the final result ('$C_1 + C_2$' curves), the cancellation stage has a non-negligible impact on the final computational burden and, as for C_1, it is linearly dependent on the number of range cells N_R. Therefore, the potential reduction of the range extent yield by the NFS configuration also provides a corresponding reduction on the contribution to the final cost.

As an example, by considering the geometry and the parameters adopted in the performed test and assuming $K = N_R$, the QMS sensor would require approximately $5.04 \cdot 10^7$ FLOPs whereas the NFS sensor processing could be implemented with $2.80 \cdot 10^7$ FLOPs. These numbers decrease to $3.92 \cdot 10^7$ FLOPs and $1.12 \cdot 10^7$ FLOPs, respectively, if the processing is optimized to include the near forward scatter area only. As is apparent, the NFS sensor configuration sets a looser constraint on the complexity of the processing architecture.

However, thanks to the optimization presented in [25], the number of FLOPs required for disturbance removal is much smaller than that needed for implementing the detection stage (map evaluation and CFAR thresholding).

Moreover, as previously noted, in the considered study case, it is mostly independent of the number of taps K. Therefore, a negligible advantage is obtained by limiting the number of taps in term of computational load of the cancellation stage. However, it is worth mentioning that, based on the reported results for the considered tests, the number of taps for the NFS sensor could be selected as smaller than 3 if a small detection loss can be accepted. With this position, the required matrix inverse could be readily evaluated even on processing architectures not tailored for such operations (e.g. GPU, FPGA, etc.).

VI. CONCLUSIONS

In this paper we presented a dedicated study aimed at investigating the feasibility of a WiFi-based passive radar for barrier coverage applications against vehicular targets. Overall the contributions of the paper can be summarized as follows.

It provides indications for a more realistic characterization of the performance of a bistatic radar Tx-Rx pair in perimeter surveillance applications. In particular it presents a detailed comparison between the QMS and the NFS acquisition geometries typically encountered in such scenarios. The comparative analysis spans from theoretical and experimental detection performance, up to the required sensor complexity.

Incidentally we observe that the experimental analysis has been performed under specific observation geometries (i.e. target crossing the Tx-Rx baseline at the mid-point and moving along an orthogonal direction) that were carefully selected to isolate the effect of the target response on the final results. This approach allowed a direct and fair comparison between the two considered sensors configurations. Indeed an extensive experimental campaign including alternative geometries would be desirable to provide a generalization of the reported results.

However, by taking into account also the considerations about the practical implementation, the reported comparison clearly show the superiority of a NFS configuration in the considered application and provide a rough but reliable quantification of the performance improvement obtained with respect to a QMS sensors configuration. In this regard, the results of this paper can be fruitfully exploited to get indications for the design of a network of sensors to be employed in barrier coverage applications.

Furthermore the paper investigates the potential exploitation of passive radar sensors for intruder detection applications. Specifically, since the transmissions for local area networking are exploited, the proposed application could be especially attractive and might play a strategic role in populated areas where WiFi signals represent a widely accessible source of opportunity. In addition it is worth noticing that the use of such illuminators potentially enables a hybrid active and passive localization of the targets based both on self-reported positions and radar measurements.

ACKNOWLEDGEMENTS

REFERENCES

[1] Special issue on bistatic and MIMO radars and their applications in surveillance and remote sensing, IET Radar Sonar & Navigation, 8, (2), 2014.

[2] Special Issue on Passive Radar (Part I&II) – IEEE Aerospace and Electronic Systems Magazine, 27, (10-11), 2012.

[3] Special Issue on Passive Radar Systems – IEE Proceedings on Radar, Sonar and Navigation, 152, (3), June 2005.

[4] F. Colone, K. Woodbridge, H. Guo, D. Mason, and C.J. Baker, "Ambiguity Function Analysis of Wireless LAN Transmissions for Passive Radar," IEEE Transactions on Aerospace and Electronic Systems, January 2011, 47, (1), pp. 240-264.

[5] F. Colone, P. Falcone, C. Bongioanni, and P. Lombardo, "WiFi-Based Passive Bistatic Radar: Data Processing Schemes and Experimental Results," IEEE Transactions on Aerospace and Electronic Systems, April 2012, 48, (2), pp. 1061-1079.

[6] K. Chetty, G.E. Smith, and K. Woodbridge, "Through-the-Wall Sensing of Personnel Using Passive Bistatic WiFi Radar at Standoff Distances," IEEE Trans. on Geoscience and Remote Sensing, April 2012, 50, (4), pp. 1218-1226.

[7] P. Falcone, F. Colone, and P. Lombardo, "Potentialities and challenges of WiFi-based passive radar," IEEE Aerospace and Electronic Systems Magazine, November 2012, 27, (11), pp. 15-26.

[8] P. Falcone, F. Colone, A. Macera, and P. Lombardo, "2D Location of Moving Targets within Local Areas using WiFi-based Multistatic Passive Radar," IET Radar Sonar and Navigation, 8, (2), pp. 123-131, Feb. 2014.

[9] F. Colone, D. Pastina, P. Falcone, P. Lombardo, "WiFi-based passive ISAR for high resolution cross-range profiling of moving targets", IEEE Transactions on Geoscience and Remote Sensing, vol. 52, no. 6, pp. 3486-3501, June 2014.

[10] D. Pastina, F. Colone, T. Martelli and P. Falcone, "Parasitic Exploitation of Wi-Fi Signals for Indoor Radar Surveillance," in IEEE Transactions on Vehicular Technology, vol. 64, no. 4, pp. 1401-1415, April 2015.

[11] B. Tan, K. Woodbridge and K. Chetty, "A wireless passive radar system for real-time through-wall movement detection," in IEEE Trans. on Aerospace and Electronic Systems, 52, (5), pp. 2596-2603, October 2016.

[12] M. Cherniakov (Ed.), Bistatic Radar: principles and practice, John Wiley & Sons, UK, 2007.

[13] M. Gashinova, L. Daniel, V. Sizov, E. Hoare and M. Cherniakov, "Phenomenology of Doppler forward scatter radar for surface targets observation," in IET Radar, Sonar & Navigation, 7, (4), pp.422-432, April 2013.

[14] M. Gashinova, L. Daniel, E. Hoare, V. Sizov, K. Kabakchiev, and M. Cherniakov, "Signal characterisation and processing in the forward scatter mode of bistatic passive coherent location systems," EURASIP Journal on Adavnces in Signal Processing, 2013.

[15] I. Suberviola, I. Mayordomo, and J. Mendizabal, "Experimental Results of Air Target Detection With a GPS Forward-Scattering Radar," in IEEE Geoscience and Remote Sensing Letters, 9, (1), pp. 47-51, Jan. 2012.

[16] P. Krysik, K. Kulpa, and P. Samczynski, "GSM based passive receiver using forward scatter radar geometry," IRS 2013, Dresden, pp. 637-642.

[17] C. Clemente, and J.J.Soraghan, "GNSS-Based Passive Bistatic Radar for Micro-Doppler Analysis of Helicopter Rotor Blades," in IEEE Trans. on Aerospace and Electronic Systems, 2014.

[18] M. Marra, A. De Luca, S. Hristov, L. Daniel, M. Gashinova and M. Cherniakov, "New algorithm for signal detection in passive FSR," 2015 IEEE Radar Conf., Johannesburg, 2015.

[19] M. Contu et alii, "Passive Multi-frequency Forward-Scatter Radar Measurements of Airborne Targets using Broadcasting Signals," in IEEE Transactions on Aerospace and Electronic Systems, PP, (99).

[20] T. Martelli, F. Colone, P. Lombardo, "First experimental results for a WiFi-based passive forward scatter radar", IEEE Radar Conf. 2016, Philadelphia (MA, USA), 2-6 May.

[21] M. I. Skolnik (Ed.), Introduction to radar systems, 3rd Edition, Tata McGraw Hill, 2001.

[22] V. Sizov, M. Cherniakov and M. Antoniou, "Forward scattering radar power budget analysis for ground targets," in IET Radar, Sonar & Navigation, 1, (6), pp. 437-446, Dec. 2007.

[23] International Telecommunication Union, ITU-R Recommendation P. 527-3: Electrical characteristics of the surface of the earth, 1992.

[24] J. I. Glaser, "Bistatic RCS of Complex Objects near Forward Scatter," in IEEE Trans. on Aerospace and Electronic Systems, AES-21, (1), pp. 70-78, Jan. 1985.

[25] F. Colone, C. Palmarini, T. Martelli, E. Tilli, "Sliding Extensive Cancellation Algorithm (ECA-S) for disturbance removal in passive radar", IEEE Trans. on Aerospace and Electronic Systems, 52, (3), pp. 1309-1326, June 2016.

[26] P. Falcone, F. Colone, and P. Lombardo, "Potentialities and challenges of WiFi-based passive radar," IEEE Aerospace and Electronic Systems Mag., 27, (11), pp. 15-26, Nov. 2012.

[27] T. Martelli, F. Colone, P. Lombardo, "First experimental results for a WiFi-based passive forward scatter radar", IEEE Radar Conf. 2016, Philadelphia (MA, USA), 2-6 May.